Applied Surface Science 572 (2022) 151361

Contents lists available at ScienceDirect

Applied Surface Science

journal homepage: www.elsevier.com/locate/apsusc

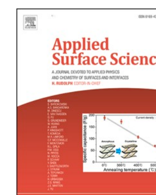

Full Length Article

First-principles investigation of structural, Raman and electronic characteristics of single layer Ge_3N_4

Y.O. Yayak [a], Y. Sozen [b], F. Tan [b], D. Gungen [a], Q. Gao [c], J. Kang [c], M. Yagmurcukardes [b,d,e,*], H. Sahin [b]

[a] *Department of Chemistry, Izmir Institute of Technology, 35430 Izmir, Turkey*
[b] *Department of Photonics, Izmir Institute of Technology, 35430 Izmir, Turkey*
[c] *Beijing Computational Science Research Center, Beijing 100193, China*
[d] *Department of Physics, University of Antwerp, Groenenborgerlaan 171, B-2020 Antwerp, Belgium*
[e] *NANOlab Center of Excellence, Groenenborgerlaan 171, B-2020 Antwerp, Belgium*

ARTICLE INFO

Keywords:
DFT-based calculations
2D Materials
semiconductors

ABSTRACT

By means of density functional theory-based first-principle calculations, the structural, vibrational and electronic properties of single-layer Ge_3N_4 are investigated. Structural optimizations and phonon band dispersions reveal that single-layer ultrathin form of Ge_3N_4 possesses a dynamically stable buckled structure with large hexagonal holes. Predicted Raman spectrum of single-layer Ge_3N_4 indicates that the buckled holey structure of the material exhibits distinctive vibrational features. Electronic band dispersion calculations indicate the indirect band gap semiconducting nature of single-layer Ge_3N_4. It is also proposed that single-layer Ge_3N_4 forms type-II vertical heterostructures with various planar and puckered 2D materials except for single-layer GeSe which gives rise to a type-I band alignment. Moreover, the electronic properties of single-layer Ge_3N_4 are investigated under applied external in-plane strain. It is shown that while the indirect gap behavior of Ge_3N_4 is unchanged by the applied strain, the energy band gap increases (decreases) with tensile (compressive) strain.

1. Introduction

Group-IV nitrides have drawn attention because of their easy accessibility, low-cost preparation, chemical stability and electrically tunability. Germanium nitride (Ge_3N_4), a member of group-IV nitrides, has been widely studied for a long time and was first experimentally realized by reacting metallic germanium and ammonia gas at high temperatures in 1930 [1]. After that, various experimental methods have been developed in order to synthesize different phases of Ge_3N_4 [2–6]. While the cubic phase of Ge_3N_4 was synthesized using laser-heated diamond anvil cell [3], its γ-phase was demonstrated by controlling the pressure and temperature in α- and β-phases [4].

The electronic and optical properties of the synthesized phases of bulk Ge_3N_4, which are large-gap semiconductors, have been studied by means of theoretical simulations [7–12]. Molina et al. investigated the properties of five different phases of Ge_3N_4 and β-Ge_3N_4 was reported to be the most stable phase among them [7]. Spinel germanium nitrides can be considered as multifunctional materials with their large exciton binding energies and tunable band gaps [11]. Among α-, β-, and γ-Ge_3N_4 phases, the β-Ge_3N_4 was reported to be a direct band gap semiconductor [12]. In addition, the thermal conductivity of γ-Si_3N_4 and γ-Ge_3N_4 were studied by comparing to that of β-Si_3N_4 and it was shown that both γ-Si_3N_4 and γ-Ge_3N_4 exhibit higher thermal conductivity at room temperature with less anisotropy [13]. In another study, both experimental and computational methods were used in order to investigate the potential of group-IV nitrides as optoelectronic materials and it was found that the Ge_3N_4 has lower electron effective masses compared to that of γ-Si_3N_4 [14–18]. Moreover, Maeda et al. reported that ultrathin Ge_3N_4 was used to create Ag/Ge_3N_4/Ge metal–insulator-semiconductor device that exhibits capacitance–voltage characteristics with no hysteresis [15]. The properties of Au/Ge_3N_4/Ge capacitors were also studied and it was found that the gate leakage current density is lower compared to that of poly-Si/SiO_2/Si while being thermally stable at higher temperatures [16]. Other applications of Ge_3N_4 includes solar cell design and photocatalyst in water splitting process. It was also proposed that adsorption of RuO_2 to β-Ge_3N_4 surface created a non-oxide photocatalysts for overall water splitting as oxygen evolution reaction occurs on the surface of β-Ge_3N_4 whereas hydrogen evolution reaction tends to

* Corresponding author at: Department of Physics, University of Antwerp, Groenenborgerlaan 171, B-2020 Antwerp, Belgium.
E-mail address: mehmetyagmurcukardes.edu@gmail.com (M. Yagmurcukardes).

https://doi.org/10.1016/j.apsusc.2021.151361
Received 13 May 2021; Received in revised form 9 September 2021; Accepted 19 September 2021
Available online 1 October 2021
0169-4332/© 2021 Elsevier B.V. All rights reserved.

occur on RuO_2 [19]. Enhancement by ammonia treatment of the photocatalytic activity of β-Ge_3N_4 in water splitting process was reported [20]. Recently, a solar cell design was proposed where spinel Ge_3N_4 and Si_3N_4 were used as solar cell absorber materials [21].

Over the last two decades, low-dimensional materials have been paid a lot of attention in material science and engineering. The discovery of graphene was though to be a milestone in science [22], and various graphene-like 2D materials, such as transition metal dichalcogenides (TMDs) [23–32], Xenes [33–39], hexagonal boron nitride (h-BN) [40] have been added to the 2D family. In order to produce smaller devices, thin, stable, durable and electrically tunable materials are required. Although, various nanostructural forms of germanium nitrides, such as nanobelts, have been reported in the sizes of 30 to 300 nm in width both in α-Ge_3N_4 and β-Ge_3N_4 phases [41–43], its 2D single-layer form has not been investigated to date.

In this work, two-dimensional form of Ge_3N_4 was investigated by means of *ab initio* calculations. The rest of the paper is organized as follows; Computational methodology is given in Section 2. Structural properties are given in Section 3.1. Vibrational properties are discussed in Section 3.2. In addition, results of the electronic properties are presented in Section 3.3 and strain-dependent electronic band dispersions are given in Section 3.4. Lastly, we concluded our results in Section 4.

2. Computational Methodology

First-principles calculations were performed based on density functional theory (DFT) as implemented the Vienna ab initio Simulation Package (VASP) [44,45]. For the exchange–correlation functional, Generalized Gradient Approximation (GGA) in the form of Perdew-Burke-Ernzerhof (PBE) was considered [46]. The projector augmented wave (PAW) potentials were used as pseudopotential datasets [47]. The van der Waals (vdW) interaction was included in the form of DFT-D2 method of Grimme [48]. Bader technique was employed to investigate the charge transfer between atoms [49].

The kinetic energy cutoff and the convergence criterion for the total energy was set to 520 eV and 10^{-5} eV, respectively. 15 Å vacuum spacing was inserted in order to avoid adjacent layer-layer interactions in the z-axis. For the structural optimization of the primitive unit cell, a $5 \times 5 \times 1$ k-point mesh was used, and it was doubled for accurate density of states calculations. In order to achieve the fully relaxed structure, pressures on each direction of the unit cell was reduced below 1 kB. The Heyd-Scuseria-Ernzerhof (HSE06) functional was employed so as to estimate experimental electronic band structure better [50]. The cohesive energy per atom was calculated using the below;

$$E_{Coh} = \frac{n_{Ge}E_{Ge} + n_N E_N - E_{sys}}{n_{tot}} \tag{1}$$

where n_{Ge} is the number of Ge atoms in the system, n_N is the number of N atoms in the system, n_{tot} is the total number of atoms in the system, E_{Ge} is the energy of a single Ge atom, E_N is the energy of a single N atom and E_{sys} is the total energy of the system.

The vibrational properties were investigated via PHON code, which uses the small displacement method [51]. For the investigation of Raman activities of phonon modes, we calculated the polarizability of crystal lattice by taking the derivative of the macroscopic dielectric tensor with respect to the finite-difference method [52].

In order to simulate STM images, partial charge densities of the primitive unit cell in the range [−3,0] eV were calculated, results were postprocessed by using Equation 2 which is based on STM working principles and employed in our recent works [53–55].

$$E_{total} = \sum_{n}^{h} E_n e^{-kz_n} \tag{2}$$

where E_{total} is the summed charge density matrix, n is the array element in z-axis, h is the total number of array elements in z-axis, E_n is the partial charge density matrix fo the nth array element, k is a constant, and z_n is the distance from the artificial STM tip in the z direction. 2D array E_{total} is converted into 8-bit image, 4×4 average filter is applied in order to improve the image quality, and visualized using custom colormap.

3. Results

3.1. Structural Properties

Crystal structure of the single-layer Ge_3N_4, which is shown in Fig. 1, is formed by a primitive unit cell containing six germanium and eight nitrogen atoms. As viewed from the side perspective, Ge_3N_4 contains two Ge-atomic layers and four N-atomic layers forming a buckled structure. The corresponding space group symmetry of single layer Ge_3N_4 is $P-3$. The optimized in-plane lattice parameter of Ge_3N_4 is $\vec{a} = \vec{b}$ =8.16 Å. The corresponding Ge-N bond lengths are found to vary between 1.85 and 2.03 Å. Moreover, the thickness of single-layer Ge_3N_4, defined as the distance between the outer-most N atoms, is found to be 2.79 Å. In order to have a better understanding on single layer Ge_3N_4, the results are compared with those for single layer C_3N_4, another member of 2D nitrate family. The optimized lattice parameter of Ge_3N_4 (8.16 Å) is found to be larger than that of g-C_3N_4 (7.15 Å) as a consequence of longer Ge-N bonds. Indeed, such larger bond length and lattice parameter result in smaller cohesive energy for single layer Ge_3N_4 indicating less energetic stability of the structure [56]. Note that, a detailed information about the atomic positions and the optimized structure is given in the Supplementary Information. Bader analysis shows that single-layer Ge_3N_4 structure is formed such that each Ge atom donates 1.8 e^- while each N atom recieves 1.3 e^- charge, indicating ionic bond character in the structure. Furthermore, the cohesive energy (E_{Coh}) is found to be 4.08 eV/atom. As compared to well-known 2D materials, such as graphene (10.04 eV/atom) and MoS_2 (9.53 eV/atom), single-layer Ge_3N_4 has a much lower cohesive energy indicating its less energetic stability [57]. In addition on the other hand, the cohesive energy of Ge_3N_4 is lower than that of predicted single-layer nitrides, BN (8.83 eV/atom), AlN (7.15 eV/atom), GaN (6.37 eV/atom), and InN (5.47 eV/atom) [57]. Furthermore, the work function of Ge_3N_4 is calculated to be higher than that of g-C_3N_4 (6.38 eV for Ge_3N_4 and 4.82 eV for g-C_3N_4) [58] stating that the electrons are mostly localized in single layer Ge_3N_4 and it is chemically more stable than g-C_3N_4 in terms of the electron exchange from the layer.

Mechanical properties of single-layer Ge_3N_4 are calculated in terms of its in-plane stiffness (C) and the Poisson ratio (ν). The calculated in-

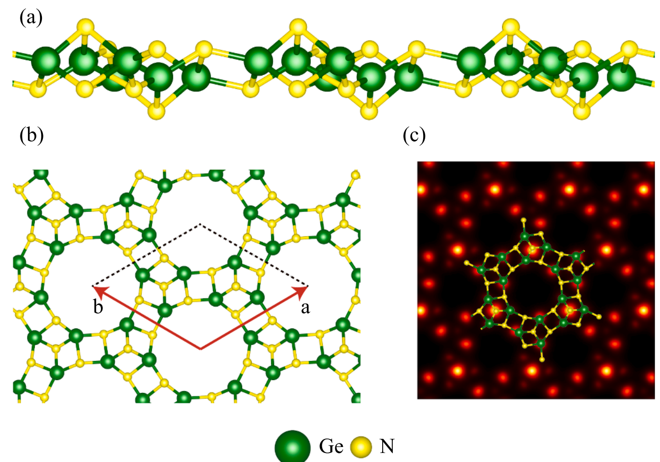

Fig. 1. For the single-layer of Ge_3N_4; (a) Side and (b) top views of the crystal structure. (c) The simulated STM image.

plane stiffness of single-layer Ge_3N_4 is 62 N/m. As compared to the stifness of well-known single-layers such as MoS_2 (122 N/m) [59] and graphene (340 N/m) [60], single-layer Ge_3N_4 is a soft material. On the other hand, while the stiffness of Ge_3N_4 is lower than that of other nitrides (267, 116, and 110 N/m for BN, AlN, and GaN, respectively), it is comaprable to that of InN (67 N/m) [57]. In addition, the Poisson ratio of a material, which is the measure of expansion perpendicular to the direction of compression, has to be between −1 to 0.5 for a stable, linear elastic material [61]. the Poisson ratio of single-layer Ge_3N_4 is found to be 0.24 and it is between that of MoS_2 (0.26) [59] and graphene (0.19) [60]. As compared to planar single-layers of nitrides, Poisson ratio of Ge_3N_4 is higher than that of BN (0.21) while it is much smaller than Poisson ratio of AlN (0.46), GaN (0.48), and InN (0.59) indicating mechanical stability of Ge_3N_4 over other nitride single-layers [57]. In addition, as compared to that of g-C_3N_4 (0.23), the Poisson ratio of Ge_3N_4 is almost the same which can be related to the crystal structure similarity [56].

3.2. Vibrational Properties

In this section, we extend our predictions by confirming the dynamical stability and investigating the lattice dynamics of the free-standing Ge_3N_4 crystal structure through the phonon band spectrum calculations. In order to obtain phonon branches, force constant matrix is generated by the implementation of small displacement method. It is seen that all phonon branches display completely positive phonon eigenvalues through the whole high-symmetry points as presented in Fig. 2(a), indicating the dynamical stability of free-standing Ge_3N_4 in its ground-state structure. The total 42 phonon branches of single-layer Ge_3N_4 include 13 doubly-degenerate and 13 non-degenerate optical branches as a result of the $P-3$ space symmetry of the structure. The highest frequency optical phonon branch is found to have a frequency of 869 cm^{-1} at the Γ point, which is much lower than that of BN, in contrast, larger than those for AlN, GaN, and InN indicating quite stronger Ge-N bonds in Ge_3N_4 [57].

The Raman activities of Γ-centered phonon modes are investigated by means of first-order off-resonant Raman calculations, which is suitable for the characterization of the material. As presented in Fig. 2(a) (right-panel), totally 13 optical branches are found to be Raman active. Among the 13 Raman active modes, we characterize the most prominent 8 phonon modes in terms of their atomic vibrations. The illustrated vibrational motions (see Fig. 2b) reveal that 4 of the Raman active modes correspond to purely in-plane while 2 of them arise from the out-of-plane vibrations of the atoms. In addition, there are also 2 Raman active modes which consist of coupled in-plane and out-of-plane vibrations. The Raman modes having in-plane vibrational character have frequencies of 223.5, 390.8, 611.0, and 850.7 cm^{-1}. The phonon modes at frequencies 850.7 and 390.8 cm^{-1} are dominated by the vibrations of the inner N atoms, while the peak at 611.0 cm^{-1} mainly arises from vibration of the outer N atoms. Moreover, the lowest frequency in-plane mode (at 235.5 cm^{-1}) stands for the rotational motion of neighboring Ge groups. On the other hand, among the out-of-plane Raman active vibrations, the peak at 589.2 cm^{-1} arises from pure outer N oscillations. In contrast, the phonon mode having frequency of 372.9 cm^{-1} is dominated by the inner N vibrations with slightly weak contribution of outer N atoms. Furthermore, the Raman active modes at 320.0 and 462.7 cm^{-1} correspond to the coupled vibrations of Ge (in-plane) and N (out-of-plane) atoms vibrations. For further analysis of the atomic contributions to the phonon vibrations, the partial phonon density of states are calculated (see Fig. S3 in Supplementary Information). Similar to the atomic weight factors calculated by Chen et al. [62], atomic-based phonon density of states give information about the atomic contributions to the vibrations. Apparently, the phonon modes below the frequency 300 cm^{-1} are dominated by the Ge-vibrations while the optical phonons above 300 cm^{-1} mostly arise from N-vibrations. The analysis of the Raman spectrum of single-layer Ge_3N_4 provide deep analysis about the characteristic of its structure.

3.3. Electronic Properties

Electronic properties of single-layer Ge_3N_4 are investigated in terms of the electronic band dispersions. As shown in Fig. 3, the valence band maximum (VBM) resides between the Γ-M points of the Brillouin Zone while the conduction band minimum (CBM) is located at the Γ point, indicating the indirect band gap nature of single-layer Ge_3N_4. The electronic band dispersions reveal that the top valence states are only dispersive around the Γ point while they are mostly localized through the M-K points. The electronic band gap is calculated to be 3.27 eV. As compared to the predicted electronic band gaps of α-, β-, and γ-Ge_3N_4 phases (3.85 eV, 3.86 eV and 3.56 eV, respectively), single-layer Ge_3N_4 possesses a slightly smaller band gap [12]. In addition, the electronic band gap of single-layer Ge_3N_4 is much smaller than the experimentally observed band gap of γ-Ge_3N_4 (4.50 eV) [5]. It is seen that the dimensional reduction from bulk to 2D structure results in the decrease of the electronic band gap. Moreover, the work function of the predicted single-layer Ge_3N_4 is calculated to be 6.38 eV which is much larger than those for single-layers of MoS_2 (5.10 eV) and h-BN (4.70 eV) [40]. Apparently, the higher work function of single-layer Ge_3N_4 indicates the localized characteristics of the electron at the top valence state. (see Table 1).

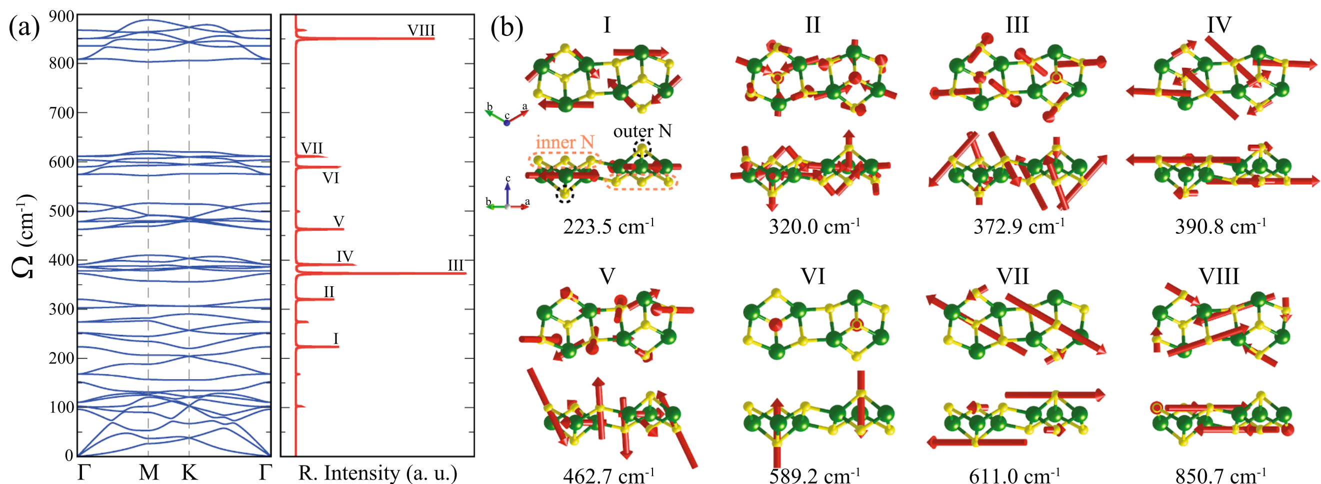

Fig. 2. For the single-layer of Ge_3N_4; (a) predicted phonon band structure (left panel) and the corresponding Raman activity of zone-centered vibrations (right panel). (b) Illustrated atomic vibrations of various Raman active phonon modes.

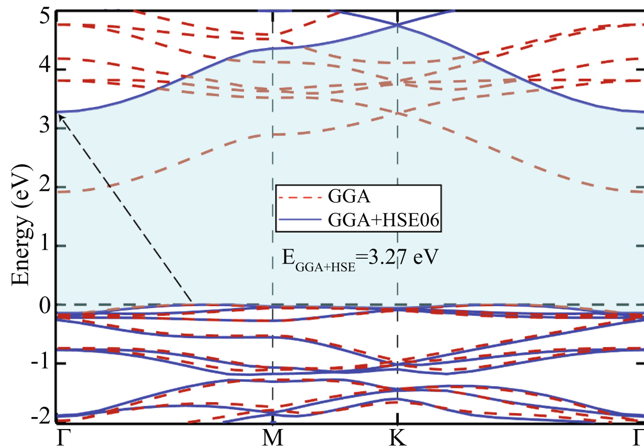

Fig. 3. Electronic band structure of single-layer Ge_3N_4. Red dashed lines belong to bare GGA band structure while blue lines represent band structure calculated with GGA + HSE06.

Experimental studies have demonstrated that single-layer 2D materials can be used as the building blocks for the formation of van der Waals type heterostructures in order to combine thier electronic properties in a single 2D structure. Fig. 4 shows the band alignment of single-layer Ge_3N_4 with several typical 2D single-layers. As shown in Fig. 4, the vacuum level of each single-layer is set to zero energy. After the shift of band edge energies by the vacuum energy, the CBM and VBM energies of Ge_3N_4 are found to be −4.33 and −7.49 eV from HSE06, and −4.69 and −6.6 eV from PBE, respectively. In order to make a general conclusion, various single-layer materials from different 2D groups are considered. MoS_2, a famous member of TMDs, GeSe and B-P are choosen as the non-planar single-layers while graphene-like planar structures of *h*-BN, GaN, and C_2N are considered as one-atom-thick materials. It is seen that the VBM energy of single-layer Ge_3N_4 is lower than that of other 2D materials considered in our study. Note that while the band gap energy of each single-layer changes with the inclusion of HSE06 in the calculations, the type of the band alignment is not affected by the functional. As shown in Fig. 4, single-layer Ge_3N_4 is predicted to form type-II band aligment with all 2D materials except for single-layer GeSe whose VBM and CBM energies are higher than those of Ge_3N_4. This facilitates the separation of electron and holes in van der Waals heterostructures constructed by Ge_3N_4 and these 2D materials, with electron localized on the Ge_3N_4 layer and hole localized on the other layer. In contrast, the GeSe-Ge_3N_4 heterostructure forms a type-I band alignment in which both electron and hole are localized on single-layer Ge_3N_4.

3.4. Strain-dependent properties

Strain is often present in experiments occuring either naturally or controllably and it can alter the electronic properties of materials. Since it is an easy and effective method, strain has often been used to manipulate fundamental properties of ultra-thin materials [63,64]. In the present section, we present our results on how the electronic structure of single-layer Ge_3N_4 responds against applied uniaxial and biaxial strains. For the investigation of uniaxial strain effect, a rectangular unit cell containing 28-atoms is constructed in order to simulate the strain along the two main orientations in the lattice, namely zigzag (ZZ) and armchair (AC) directions (see Fig. 5(a)).

Effects of uniaxial as well as biaxial strains on the electronic band

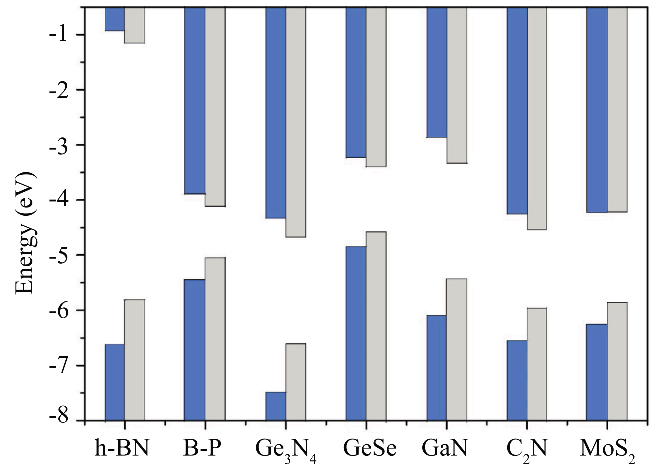

Fig. 4. Band alignment between Ge_3N_4 and several typical 2D materials. Blue and gray bars indicate results calculated by HSE06 and PBE, respectively. The vacuum energy is set as zero.

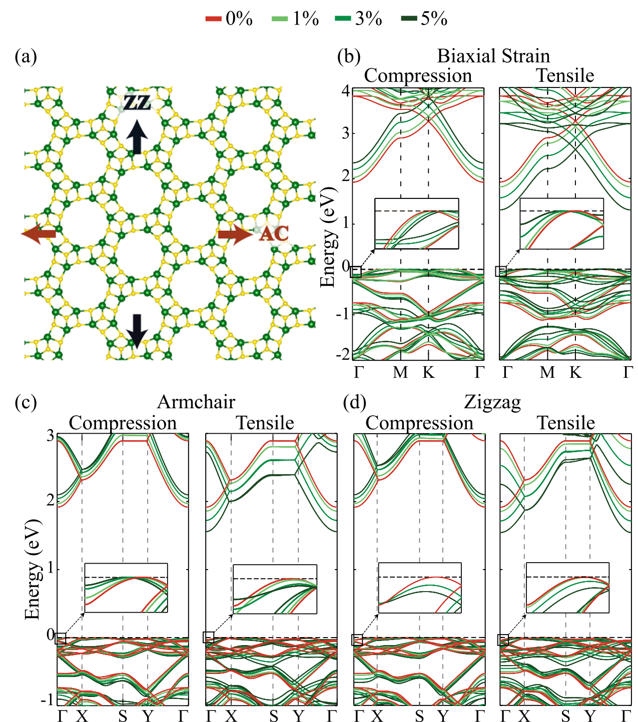

Fig. 5. (a) AC and ZZ orientations of single-layer Ge_3N_4 with rectangular unit cell. The electronic band diagrams of single-layer Ge_3N_4 under (b) biaxial strain, (c) uniaxial strain on AC orientation, (d) uniaxial strain on ZZ orientation.

Table 1
For the single-layer of G_3N_4; optimized in-plane lattice parameter, *a*; the vertical distance between the outer-most N atoms, *h*; the amount of charge donated by a Ge atom and received by a N atom, ρ_{Ge} and ρ_N; the work function, ϕ; calculated cohesive energy per atom, E_{Coh}; electronic band gaps calculated within GGA and HSE06 functionals, E_{Gap} and E_{Gap}^{HSE06}; and the linear-elastic parameters, in-plane stiffnes (*C*) and Poisson ratio (ν).

	a	h	ρ_{Ge}	ρ_N	ϕ	E_{Coh}	E_{Gap}	E_{Gap}^{HSE06}	C	ν
	(Å)	(Å)	(e^-)	(e^-)	(eV)	(eV/atom)	(eV)	(eV)	(N/m)	-
Ge_3N_4	8.16	2.79	1.8	1.3	6.38	4.08	1.92	3.27	62	0.24

dispersions are calculated by changing the lattice parameters by ± 1 %, ± 3 % and ± 5 % amounts both in tensile and compressive cases. The results for the biaxial strain are presented in Fig. 5(b). It is seen that the CBM of single-layer Ge_3N_4 displays shift to lower energies via applied tensile biaxial strain while it shifts to higher energies under compressive strain. As a result of those shifts of the CBM, the electronic band gap is found to change from 1.30 eV (at 5% of tensile biaxial strain) to 2.34 eV (at 5% of compressive biaxial strain). Note that the indirect gap behavior of Ge_3N_4 is robust against the applied biaxial strain regardless of the strain type, compressive or tensile. In addition, while the location of VBM does not change via biaxial strain, the energy of the valence states at the Γ point increases under tensile strain resulting in less dispersive states residing between the Γ-M points.

On the other hand, our results for the applied uniaxial strains are shown in Figs. 5(c) and (d) (for AC and ZZ directions, respectively). Note that since a rectangular cell is used for the uniaxial strain, the high symmetry points are given in the corresponding frame. For the applied strain types and strain ranges, the obtained stress–strain curves (see Fig. S2 of Supplementary Information) reveal that the structures fall into elastic limits in terms of their elastic stabilities. Therefore, the applied strain strengths are meaningful such that the structures do not undergo an elastic deformation. It is seen that regardless of the strain direction, the energy of the CBM displays a shift to higher (lower) energies via applied compressive (tensile) strain. However, in all cases the CBM resides at the same point under applied uniaxial strain. As zoomed out in the insets of Figs. 5(c) and (d), the compressive uniaxial strain along AC direction exhibits a similar effect with that of tensile biaxial strain for the valence state residing between the Γ-M points. It is found that the electronic band gap decreases (increases) via uniaxial tensile (compressive) strains. The energy band gap ranges from 1.56 eV (at 5% of tensile uniaxial strain) to 2.10 eV (at 5% of compressive uniaxial strain) in both directions. It is clear that the indirect nature of the electronic band gap is not affected by the type or direction of the uniaxial strain while the band gap changes depending on the strength of the strain. The mechanism behind such change can be found in the atomic orbital contributions to the lowest conduction and highest valence states. It is found that the CBM state is formed by the in-plane orbitals of the atoms, which indicates that those states are more sensitive to the applied in-plane strain. In contrast, the VBM state is dominated by the out-of-plane orbitals of the individual atoms and thus, VBM is mostly unaffected by the in-plane strain.

4. Conclusions

In summary, we performed DFT-based first-principles calculations in order to investigate the structural, vibrational and electronic properties of single-layer Ge_3N_4 and the effects of biaxial and uniaxial strains on the electronic properties were reported. Geometry optimization revealed that single-layer Ge_3N_4 possesses a holey buckled structure. Phonon band dispersion calculations showed that single-layer Ge_3N_4 is dynamically stable. Further investigations on vibrational properties indicated that Raman active phonon modes can be used as key for the identification of single-layer Ge_3N_4 via Raman spectroscopy. Moreover, the electronic properties of single-layer Ge_3N_4 were investigated in terms of the electronic bands and it was shown that Ge_3N_4 is a large gap semiconductor with an indirect band gap behavior. In addition, it was also predicted that single-layer Ge_3N_4 forms type-II vdW heterostructures with various one-atom-thick and puckered 2D materials except for single-layer GeSe which gives rise to a type-I band alignment. Furthermore, it was found that independent of the type of the applied strain, biaxial or uniaxial, single-layer Ge_3N_4 preserves its indirect gap nature while its electronic band gap is tunable with external strain. Single-layer Ge_3N_4 can be considered as a potential candidate for nanoelectronic applications with its strain-tunable band gap.

Declaration of Competing Interest

The authors declare that they have no known competing financial interests or personal relationships that could have appeared to influence the work reported in this paper.

Acknowledgments

Computational resources were provided by TUBITAK ULAKBIM, High Performance and Grid Computing Center (TR-Grid e-Infrastructure). H.S. acknowledges support from Türkiye Bilimler Akademisi - Turkish Academy of Sciences under the GEBIP program. M.Y. was supported by a postdoctoral fellowship from the Flemish Science Foundation (FWO-Vl). The data that support the findings of this study are available from the corresponding author upon request.

Appendix A. Supplementary material

Supplementary data associated with this article can be found, in the online version, at https://doi.org/10.1016/j.apsusc.2021.151361.

References

[1] W.C.J. Johnson, Am. Chem. Soc 52 (1930) 5160–5165.
[2] H. He, T. Sekine, T. Kobayashi, K.J. Kimoto, Appl. Phys 90 (2001) 4403–4406.
[3] G. Serghiou, G. Miehe, O. Tschauner, A. Zerr, R.J. Boehler, Chem. Phys 111 (1999) 4659–4662.
[4] Leinenweber, K.; O'keeffe, M.; Somayazulu, M.; Hubert, H.; McMillan, P.; Wolf, G. Chem-Eur. J 1999, 5, 3076–3078.
[5] T. Maeda, T. Yasuda, M. Nishizawa, N. Miyata, Y. Morita, S.J. Takagi, Appl. Phys 100 (2006) 014101.
[6] N. Nishiyama, J. Langer, T. Sakai, Y. Kojima, A. Holzheid, N.A. Gaida, E. Kulik, N. Hirao, S.I. Kawaguchi, T.J. Irifune, Am. Ceram. Soc 102 (2019) 2195–2202.
[7] B. Molina, L. Sansores, Int. J. Quantum Chem 80 (2000) 249–257.
[8] C. Sevik, C.J. Bulutay, Mater. Sci 42 (2007) 6555–6565.
[9] I.-H. Chu, A. Kozhevnikov, T.C. Schulthess, H.-P.J. Cheng, Chem. Phys 141 (2014) 044709.
[10] S.-P. Gao, G. Cai, Y. Xu, Comp. Mater. Sci 67 (2013) 292–295.
[11] T. Boyko, A. Hunt, A. Zerr, A. Moewes, Phys. Rev. Lett 111 (2013) 097402.
[12] B.H.D. Jayatunga, W.R. Lambrecht, Phys. Rev. B 102 (2020) 195203.
[13] H. Xiang, Z. Feng, Z. Li, Y. Zhou, Sci. Rep-UK 8 (2018) 1–9.
[14] C.M. Caskey, J.A. Seabold, V. Stevanović, M. Ma, W.A. Smith, D.S. Ginley, N. R. Neale, R.M. Richards, S. Lany, A.J. Zakutayev, Mater. Chem. C 3 (2015) 1389–1396.
[15] T. Maeda, T. Yasuda, M. Nishizawa, N. Miyata, Y. Morita, S. Takagi, Appl. Phys. Lett 85 (2004) 3181–3183.
[16] G. Okamoto, K. Kutsuki, T. Hosoi, T. Shimura, H.J. Watanabe, Nanosci. Nanotechno 11 (2011) 2856–2860.
[17] G. Lucovsky, S. Lee, J. Long, H. Seo, J. Lüning, App. Surf. Sci 254 (2008) 7933–7937.
[18] R. Lieten, V. Afanas'ev, N. Thoan, S. Degroote, W. Walukiewicz, G.J. Borghs, Electrochem. Soc 158 (2011) H358.
[19] Y. Ma, M. Wang, X.J. Zhou, Energy Chem 44 (2020) 24–32.
[20] Y. Lee, T. Watanabe, T. Takata, M. Hara, M. Yoshimura, K. Domen, J. The, Phys. Chem. B 110 (2006) 17563–17569.
[21] P. Sánchez-Palencia, G. García, J.C. Conesa, P. Wahnón, P. Palacios, Acta Mater 197 (2020) 316–329.
[22] Novoselov, K.S.; Geim, A.K.; Morozov, S.V.; Jiang, D.; Zhang, Y.; Dubonos, S.V.; Grigorieva, I.V.; Firsov, A.A. science 2004, 306, 666–669.
[23] M. Chhowalla, H.S. Shin, G. Eda, L.-J. Li, K.P. Loh, H. Zhang, Nat. Chem 5 (2013) 263–275.
[24] Q.H. Wang, K. Kalantar-Zadeh, A. Kis, J.N. Coleman, M.S. Strano, Nat. Nanotechnol 7 (2012) 699–712.
[25] J.S. Ross, P. Klement, A.M. Jones, N.J. Ghimire, J. Yan, D. Mandrus, T. Taniguchi, K. Watanabe, K. Kitamura, W. Yao, D.H. Cobden, X. Xu, Nat. Nanotechnol 9 (2014) 268–272.
[26] K.F. Mak, C. Lee, J. Hone, J. Shan, T.F. Heinz, Phys. Rev. Lett 105 (2010) 136805.
[27] S. Tongay, J. Zhou, C. Ataca, K. Lo, T.S. Matthews, J. Li, J.C. Grossman, J. Wu, Nano Lett. 12 (2012) 5576–5580.
[28] T. Georgiou, R. Jalil, B.D. Belle, L. Britnell, R.V. Gorbachev, S.V. Morozov, Y.-J. Kim, A. Gholinia, S.J. Haigh, O. Makarovsky, L. Eeves, L.A. Ponomarenko, A. K. Geim, K.S. Novoselov, A. Mishchenko, Nat. Nanotechnol 8 (2013) 100–103.
[29] A. Ramasubramaniam, Phys. Rev. B 86 (2012) 115409.
[30] B. Radisavljevic, A. Radenovic, J. Brivio, V. Giacometti, A. Kis, Nat. Nanotechnol 6 (2011) 147–150.
[31] H. Fang, S. Chuang, T.C. Chang, K. Takei, T. Takahashi, A. Javey, Nano Lett 12 (2012) 3788–3792.
[32] S. Tongay, et al., Nat. Commun 5 (2014) 1–6.

[33] A. Molle, J. Goldberger, M. Houssa, Y. Xu, S.-C. Zhang, D. Akinwande, Nat. Mater 16 (2017) 163–169.
[34] P. Vogt, P. De Padova, C. Quaresima, J. Avila, E. Frantzeskakis, M.C. Asensio, A. Resta, B. Ealet, G. Le Lay, Phys. Rev. Lett 108 (2012) 155501.
[35] X.-L. Yu, L. Huang, J. Wu, Phys. Rev. B 95 (2017) 125113.
[36] B. Cai, S. Zhang, Z. Hu, Y. Hu, Y. Zou, H. Zeng, Phys. Chem. Chem. Phys 17 (2015) 12634–12638.
[37] L. Matthes, O. Pulci, F. Bechstedt, New J. Phys 16 (2014) 105007.
[38] H. Şahin, S. Cahangirov, M. Topsakal, E. Bekaroglu, E. Akturk, R.T. Senger, S. Ciraci, Phys. Rev. B 80 (2009) 155453.
[39] F.-F. Zhu, W.-J. Chen, Y. Xu, C.-L. Gao, D.-D. Guan, C.-H. Liu, D. Qian, S.-C. Zhang, J.-F. Jia, Nat. Mater 14 (2015) 1020–1025.
[40] L.H. Li, Y. Chen, Adv. Funct. Mater 26 (2016) 2594–2608.
[41] Y. Gao, Y. Bando, T. Sato, Appl. Phys. Lett 79 (2001) 4565–4567.
[42] T. Xie, Z. Jiang, G. Wu, X. Fang, G. Li, L.J. Zhang, Cryst. Growth 283 (2005) 286–290.
[43] D. Jishiashvili, L. Kiria, Z. Shiolashvili, N. Makhatadze, E. Miminoshvili, A. J. Jishiashvili, Nanosci (2013) 2013.
[44] G. Kresse, J. Hafner, Phys. Rev. B 47 (1993) 558.
[45] G. Kresse, J. Furthmüller, Phys. Rev. B 54 (1996) 11169.
[46] J.P. Perdew, K. Burke, M. Ernzerhof, Phys. Rev. Lett 77 (1996) 3865.
[47] P.E. Blöchl, Phys. Rev. B 50 (1994) 17953.
[48] S. Grimme, J. Antony, S. Ehrlich, H.J. Krieg, Chem. Phys 132 (2010) 154104.
[49] G. Henkelman, A. Arnaldsson, H. Jónsson, Comp. Mater. Sci 36 (2006) 354–360.
[50] J. Heyd, G.E.J. Scuseria, Chem. Phys 121 (2004) 1187–1192.
[51] D. Alfè, Comput. Phys. Commun 180 (2009) 2622–2633.
[52] Placzek, G. The rayleigh and raman scattering; Lawrence Radiation Laboratory, 1959; Vol. 526.
[53] G. Binnig, H. Rohrer, C. Gerber, E. Weibel, Appl. Phys. Lett. 40 (1982) 178–180.
[54] R. Plumadore, M. Baskurt, J. Boddison-Chouinard, G. Lopinski, M. Modarresi, P. Potasz, P. Hawrylak, H. Sahin, F.M. Peeters, A. Luican-Mayer, Phys. Rev. B 102 (2020) 205408.
[55] E. Ceyhan, M. Yagmurcukardes, F. Peeters, H. Sahin, Phys. Rev. B 103 (2021) 014106.
[56] L.-H. Qu, Z.-Y. Deng, J. Yu, X.-K. Lu, C.-G. Zhong, P.-X. Zhou, T.-S. Lu, J.-M. Zhang, X.-L. Fu, Vacuum 176 (2020) 109358.
[57] H. Şahin, S. Cahangirov, M. Topsakal, E. Bekaroglu, E. Akturk, R.T. Senger, S. Ciraci, Physical Review B 80 (2009) 155453.
[58] K. Bai, Z. Cui, E. Li, Y. Ding, J. Zheng, C. Liu, Y. Zheng, Vacuum 175 (2020) 109293.
[59] M. Yagmurcukardes, R. Senger, F. Peeters, H. Sahin, Phys. Rev. B 94 (2016) 245407.
[60] C. Lee, X. Wei, J.W. Kysar, Hone J. science 321 (2008) 385–388.
[61] H. Gercek, Int. J. Rock Mech. 44 (2007) 1–13.
[62] X.-K. Chen, X.-Y. Hu, P. Jia, Z.-X. Xie, J. Liu, Int. J. Mech. Sci. (2021) 106576.
[63] M. Yagmurcukardes, C. Bacaksiz, E. Unsal, B. Akbali, R. Senger, H. Sahin, Phys. Rev. B 97 (2018) 115427.
[64] E. Torun, H. Sahin, S. Cahangirov, A. Rubio, F.J. Peeters, Appl. Phys 119 (2016) 074307.